



A combined multiphysics modeling and deep learning framework to predict thermal runaway in cylindrical Li-ion batteries



Basab Ranjan Das Goswami^a, Massimiliano Mastrogiovio^b, Marco Ragone^b, Vahid Jabbari^b, Reza Shahbazian-Yassar^b, Farzad Mashayek^a, Vitaliy Yurkiv^{a,*}

^a Department of Aerospace and Mechanical Engineering, University of Arizona, Tucson, AZ, 85721, USA

^b Department of Mechanical and Industrial Engineering, University of Illinois at Chicago, Chicago, IL, 60607, USA

HIGHLIGHTS

- Multiphysics modeling of thermal runaway (TR).
- Simulated battery thermal imaging for training machine learning models for TR detection.
- Multiclass classification of TR evolution: safe, critical, and TR stages.
- Real-time detection of TR heat sources using object detection.

ARTICLE INFO

Keywords:

Thermal runaway
Multiphysics model
Machine learning
Deep learning
Computer vision
Real-time object detection

ABSTRACT

In this paper, machine learning (ML)/deep learning (DL) has been employed to predict the thermal runaway (TR) occurrence in Li-ion batteries (LIBs). State-of-the-art convolutional neural networks (CNNs) are adopted to forecast the evolution of the TR phenomenon with a classification approach of three distinct stages, namely, safe operation, critical condition of triggered the TR, and the actual TR occurrence. In addition, the “you look only once” (YOLO) object detection ML model is used to identify the location of the TR heat sources within the battery. The neural networks are trained on simulated thermal images, computed with the multiphysics modeling of LIBs. The multiphysics modeling approach comprises a coupled thermal, electrochemical (P2D model), and degradation sub-models. The degradation phenomenon leading to the TR considered in this paper is the solid electrolyte interface (SEI) formation/decomposition on the negative electrode. The proposed ML model exhibits high accuracy in predicting the TR evolution stages and heat source locations. The combined multiphysics and ML modeling approach developed in this work provides qualitative insights for ‘on-the-fly’ prediction of the TR, as well as a framework for extending data-driven methodologies to broad applications in electrochemistry.

1. Introduction

Li-ion batteries (LIBs) are one of the most extensively used energy storage devices and essential pillars in future energy management systems [1–3]. LIBs offer some of the highest energy and power densities (both volumetric and gravimetric) among many other energy storage technologies [4]. The safety aspects of LIBs have become increasingly crucial for reliable and long-lasting usage. However, recent events of some electric vehicle (EV) explosions [5] show the necessity to reevaluate the safety aspects of LIBs. The major bottleneck with LIBs is the occasional uncontrollable failures in both energetic and non-energetic

modes. Both modes may occur due to numerous reasons, such as cell manufacturing flaws, poor (electrical or mechanical) cell design, external (thermal, mechanical, or electrical) abuse of cells, defective protection electronics, and chargers [6]. In this work, the focus is on the most severe energetic failure [7,8] of the LIBs that occurs due to the thermal runaway (TR). In general, the TR consists of a cell’s rapid self-heating sourced from exothermic (electrochemical) reactions, mechanical abuse and/or thermal abuse [9–16]. During the TR, excessive heat has a detrimental influence on the electrical characteristics and the state-of-charge (SOC) of the LIBs. The extreme heat can cause separator decomposition causing an internal short-circuit, which itself intensifies

* Corresponding author.

E-mail address: vyurkiv@arizona.edu (V. Yurkiv).

the heat generation, leading to an accidental explosion of the battery. It is quite challenging to directly monitor the events occurring during the TR in practical operating conditions. However, the change in electrical parameters during the TR-like events could potentially indicate the existence of a failure, thus allowing to foresee the LIBs' malfunction. Predicting such unwanted TR-like events in advance and under real-life conditions is an imperative step in LIBs' eventual insertion within the next-generation energy storage technologies.

The mechanism of the TR has been reviewed in many prior publications [11,17–21]. The thermal behavior of LIBs can be described by temperature profiles based on the results of accelerating rate calorimeter (ARC) tests [18,22,23]. When the temperature increases, multiple degradation mechanisms can occur within the battery that can trigger the TR event. Inside a battery, typically, three major degradation mechanisms are observed, i.e., the SEI decomposition, Li-electrolyte reaction, and a cathode decomposition [24,25]. These reactions raise the temperature enough to cause the separator to melt down and lead to an internal short circuit in the battery, which further increases the temperature. The decomposition of the solid electrolyte interphase (SEI) is important to identify the temperature at which the cell starts self-heating [12,26–29]. When the cell temperature rises to a certain extent, first, the decomposition of the SEI layer takes place and then releases heat. The decomposition of this protective layer can trigger other exothermic reactions [28] and, ultimately, leads to thermal runaway. Therefore, understanding the evolution of the temperature due to the onset of the SEI decomposition is very important for introducing warnings for battery management systems.

There are serious safety issues for monitoring the TR event experimentally [30,31]. In this regard, researchers have put forward extensive efforts toward the development of numerical models [32] to predict the TR behavior. Richard and Dahn [24] have utilized ARC to investigate the thermal stability of lithium intercalated mesocarbon microbead (MCMB) electrodes by estimating its self-heating rate. Additionally, Richard and Dahn have presented a mechanism to elucidate the amount of heat that was generated from chemical reactions between the lithiated carbon and the electrolyte [25]. Hatchard et al. [33] drew upon this work and have built a 1D model to estimate the temperature when the TR starts for LCO/graphite cells that are subjected to an oven with a constant temperature. Then, Spotnitz and Franklin [28] have summed up the essential exothermic reactions of the battery components. They have developed a 1D model to provide quantitative insights to the contribution of heat generation from separate reactions and used it for various abuse tests. Moreover, Kim et al. [27] have broadened the model proposed by Hatchard et al. [33] to a 3D model where the TR is prompted by thermal abuse (external heating).

With many of the latest developments in artificial intelligence and data-driven algorithms, it is now possible to significantly advance the state-of-the-art in the study of LIBs and their materials. This allows a significant improvement in the performance of battery technologies to be rapidly achieved. ML has been extensively used in different areas of battery research at different length scales, from fundamental studies of structural properties to end-use applications like EVs. In the studies of structure properties, ML methods have shown to be promising techniques for the investigation of the structure-properties relationships and the understanding of the behavior of the materials employed in LIBs [34–36]. Another area of research related to LIBs and ML is the battery state-of-charge (SOC) estimation for EVs [37,38]. This has gained significant recognition in recent times due to the extensive development of EVs. Moreover, there have been significant works on the application of ML to estimate the SOH (State of Health), SOC, and RUL (Remaining Useful Life) using methods such as XGBoost, random forest, and k-nearest neighbor algorithm (KNN) [39,40]. Similarly, ML models are also applied in LIBs prognostics [41]. Additionally, ML methods, namely support vector machine (SVM), relevance vector machine (RVM) [42], and Gaussian process regression (GPR) [43,44] have been widely used in this area of research. Deep learning (DL) methods like artificial neural

networks (ANNs) [45] have been utilized in the area of battery design and health monitoring. Recently, there have been reports of DL/ML models [46,47], which include the prediction of simulated/experimental results at reduced computational costs for inspecting and forecasting battery events like the TR. Based on a thorough search, there are only a few papers in the prior literature dedicated to DL/ML usage to predict the TR in LIBs. In this regard, Yamanaka et al. [48] used nail penetration simulations on different input conditions to generate a database and used regression models to inspect the design conditions for better performance of batteries. Naha et al. [49] utilized an ML method known as a random forest classifier to detect internal short circuit (ISC) leading to the TR in batteries from simulated data as input.

Despite ML's promising capabilities, the existing literature on ML application to battery research is limited to the modeling of materials properties or SOC estimation without relating it to the degradation phenomena. Yet, learning-driven approaches for battery design and thermal runaway prediction are limited to data-driven approaches. Thus, the primary objective of this paper is to develop a combined multiphysics and ML-based approach to predict and prevent the TR in LIBs using thermal images of the battery during operation. The supporting objective is to provide the safety aspects of LIBs operation derived from the multiphysics informed ML techniques. For the multiphysics model, the Panasonic 18650 cylindrical cell has been considered. This cell utilizes Graphite as the negative electrode and NMC as the positive electrode. Since the SEI decomposition sets a pathway for thermal runaway, the SEI decomposition has been considered as the major degradation mechanism in the multiphysics model. Additionally, multiple high-temperature hotspots have been considered at different locations within the battery. From the multiphysics model, thermal images have been generated as sequences of video frames during the battery operation. Next, the extracted images are used for the application of various ML methodologies. In the ML study, a classification technique has been employed using various convolutional neural networks (CNNs) to predict the TR. For this purpose, three labels have been considered, namely, safe, critical, and the TR. The selection of these labels is solely dependent on the maximum surface temperature of the battery and has been explained in detail in the methodology section. Finally, an advanced application of ML has been utilized known as object detection [50], a technique that has not previously been used in the area of the TR, for the detection of high-temperature hotspots in the battery, which could lead to the TR.

2. Methodology

In this section, the general workflow of the study that has been carried out is described. First, a computational approach has been developed to investigate battery degradation using an electrochemical-thermal model of LIBs. This is followed by the acquisition of thermal images from the simulations after undergoing further data preprocessing. Then, these images are fed into the DL network for the classification task of predicting three labels related to the TR event. Finally, the detection of high-temperature hotspots in the battery using an object detection technique is performed. Fig. 1 shows the class of systems modeled in this work (left-hand side) together with the ML workflow (right-hand side).

2.1. Multiphysics modeling methodology

In this section, the methodology involving the multiphysics model is described. First, the general electrochemical model has been discussed followed by the description of the thermal model. Additionally, the initial and boundary conditions for the model, followed by a general introduction involving the model implementation, have been discussed. The multiphysics model utilizes the finite element method (FEM) to simulate the electrochemical-thermal behavior of a cylindrical battery type at various conditions. The P2D model [51–53] is used for modeling

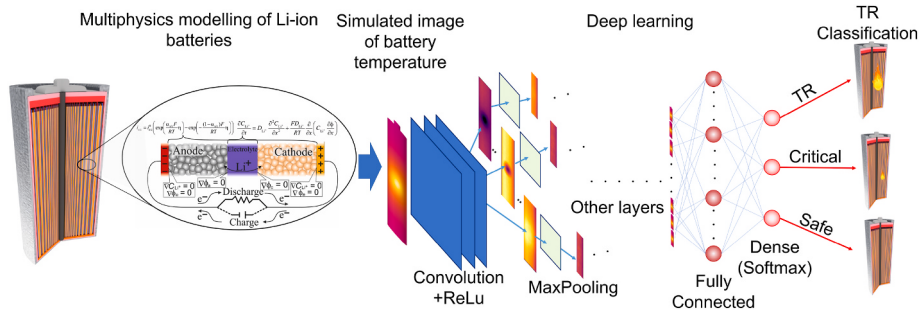


Fig. 1. Schematic illustration of physics informed ML study to predict and identify the TR in cylindrical type LIBs. The multiphysics modeling (left-hand side image) of cylindrical cell is used to create a data set for ML (middle image), allowing to identify and forecast the TR in LIBs. Note: the images on the left are not to scale, merely for illustration purposes.

electrochemistry, and a 3D model has been used to simulate the battery temperature. The two models are then coupled by the generated heat source and the temperature. Highlighting the pivotal role of the P2D model, its reputation is built on a foundation of exceptional accuracy when compared to experimental data. Doyle and Newman's influential work has unequivocally demonstrated the effectiveness of the P2D model through direct comparisons with experimental results [54]. Notably, the outcomes exhibit commendable alignment with experimental data, particularly in scenarios involving non-uniform SEI growth. This robust validation underscores the reliability and effectiveness of the P2D model in capturing real-world phenomena, further affirming its credibility in our study. A detailed description of the governing equations related to the P2D model and the corresponding boundary conditions has been provided in the supplementary information. In addition to the main graphite-lithium intercalation reaction on the negative electrode, the model considers parasitic SEI formation reaction as well. The kinetic expression for the SEI formation reaction is based on the work of Ekstrom and Linderberg [55] and has been provided in the supplementary information. It is assumed that the SEI formation is limited by a diffusion process through the formed SEI film, with the result that the aging slows down the thickening of the film. In normal operating conditions, the cell is subjected to a continuous charge/discharge load. Consequently, heat generation takes place within the cell due to various electrochemical processes. The thermal characteristics, such as heat generation due to various electrochemical reactions, in the case of the TR event can be described by the general energy conservation equation for both phases (solid and fluid) in the vector form as [53].

$$\rho C_p \frac{\partial T}{\partial t} + \rho C_p \mathbf{u} \cdot \nabla T + \nabla \cdot \mathbf{q} = Q_{\text{gen}}, \quad (1)$$

where,

$$\mathbf{q} = -k \nabla T \quad (2)$$

Here, k , is the thermal conductivity of the battery. It takes the form of a symmetric positive-definite tensor (matrix) and is given as

$$k = \begin{bmatrix} k_{\text{th}} & 0 & 0 \\ 0 & k_{\text{in}} & 0 \\ 0 & 0 & k_{\text{in}} \end{bmatrix} \quad (3)$$

where, k_{in} being the in-plane thermal conductivity and k_{th} being the through-plane thermal conductivity of the cell. In Eq. (3), ρ denotes the average density of the cell; C_p is the average specific heat capacity; T is the temperature; and Q_{gen} is the volumetric heat generation rate (HGR). The HGR of the cell is given by [56]

$$Q_{\text{gen}} = Q_{\text{elec}} + Q_{\text{SEI}}, \quad (4)$$

where, Q_{elec} is the dominant HGR from the fundamental electrochemical reactions and Q_{SEI} is the dominant HGR for the SEI decomposition re-

action. The convection term is zero in the solid phase due to the lack of a fluid motion in that phase. The total electrochemical HGR is determined by the sum of irreversible heat from Joule heating and activation losses and reversible heat from electrochemical reaction and is given by [56]

$$Q_{\text{elec}} = -(\mathbf{i}_s \bullet \nabla \varphi_s + \mathbf{i}_l \bullet \nabla \varphi_l) + \sum_m a_{v,m} \left\{ (\varphi_s - \varphi_l - E_{\text{eq},m}) i_m + T \frac{\partial E_{\text{eq},m}}{\partial T} i_m \right\}, \quad (5)$$

The variables in the electrochemical HGR are the electrode current i_s , electrolyte current i_l , electrode potential φ_s , electrolyte potential φ_l , the equilibrium voltage for each reaction $E_{\text{eq},m}$, local current due to an electrochemical reaction i_m , the active specific surface area $a_{v,m}$ and the change in equilibrium voltage with respect to the temperature for each electrode reaction $\frac{\partial E_{\text{eq},m}}{\partial T}$. It is to be noted that the variables $i_s, \varphi_s, i_l, \varphi_l$ and i_m are calculated based on the P2D equations. As previously mentioned, multiple exothermic reactions can occur inside the battery that may trigger the TR event. When the battery is in operation under charge/discharge load, reversible and irreversible reactions take place inside the battery, which releases heat and causes the temperature to rise. Along with these reactions, the SEI-forming parasitic reactions also occur in the anode of the battery. After a certain growth, the SEI undergoes a decomposition reaction, which is exothermic in nature and releases heat. The HGR due to the SEI decomposition reaction is given by [57]

$$Q_{\text{SEI}} = a_c h_{\text{SEI}} j_{\text{SEI},d}, \quad (6)$$

where, a_c is the active specific surface area; h_{SEI} is the enthalpy of the reaction and j_{SEI} represents the reaction kinetics of the SEI decomposition reaction. Detailed descriptions of the symbols and additional equations for the reaction kinetics and the corresponding degradation parameters are given elsewhere [57]. It should be noted that the SEI formation has been reported to be a complex mixture of compounds, such as LiF, Li_2CO_3 , lithium ethylene dicarbonate ($(\text{CH}_2\text{OCO}_2\text{Li})_2$, LEDC) and lithium alkyl carbonates (ROCO_2Li) [58]. During the decomposition process, these compounds may have their own series of reactions. However, due to the lack of appropriate kinetic and thermodynamic data associated with all these reactions, it is reasonable to assume one global rate-limiting step for the SEI decomposition process. The intense heat release from the SEI decomposition reaction escalates the temperature of the battery. This creates high-temperature hotspots inside the battery, whose location is completely stochastic. The appearance of such hotspots may occur due to local defects present within the structure of the battery. These local defects can form due to multiple reasons, e.g., deflected current collectors, non-uniform packing, delamination, presence of impurities in the anode/cathode, burrs on the tab [59]. Since modeling does not allow the formation of such hotspots automatically, these hotspots are introduced artificially within the battery at random locations and simulate the battery operation. These hotspots are directly associated with the degradation mechanism in

consideration. The heat release from the degradation of the battery leads to self-heating of the battery in a short period of time and causes a thermal runaway to occur. In this work, the SEI formation/decomposition has been considered as the major degradation phenomenon that leads to the TR. Additionally, the developed model is solved for the continuity and momentum equations, that are given elsewhere [60,61]. The initial and boundary conditions for the governing equations are provided in the supplementary information.

2.1.1. Model implementation

The mathematical model constitutes a multi-scale and multi-domain approach and is implemented in COMSOL Multiphysics [62]. The model uses an unstructured quadratic finite element mesh and the backward Euler scheme for time discretization purposes. The PARDISO (COMSOL, 5.6) solver for a finite element problem to solve the system of linear equations as well as for the initialization and the transient stages is used. For the simulations presented in this paper, a cylindrical 18650 cell with NMC chemistry has been chosen and a 3D model is implemented. A Graphite negative electrode, an NMC811 positive electrode, and an electrolyte 3:7 EC:EMC with a 1 M LiPF₆ salt from the COMSOL material library have been selected. The model has been simulated with a user-defined condition that when the maximum temperature of the battery exceeds 400 K, the calculations should stop. This has been implemented as the battery will undergo rapid self-heating beyond this point in a short period of time and will eventually explode. All parameters employed in the simulations presented in this paper are summarized in Table S3 of the Supplementary Information.

2.2. Deep learning methodology

The following section is dedicated to the description of the proposed DL framework, and it is structured in two parts: first, the dataset preparation and preprocessing is discussed, followed by the implementation of DL models. The section related to the implementation of the DL model is further divided into two parts. First, the classification technique used to predict the TR from the thermal images obtained from the multi-physics modeling is explained. Next, the development of the object detection technique used to identify the location of high-temperature hotspots has been introduced which eventually leads to thermal runaway.

2.2.1. Dataset preparation and preprocessing

Initially, simulated thermal images of the battery are collected as sequences of video frames during the battery operation. Such thermal images contain physical features related, for example, to the battery surface temperatures and the cooling airflow. For applying the ML techniques to predict the TR, the temperature is the main subject of discussion. From the simulation results, the thermal images of the battery are saved in a continuous time interval of battery operation, considering a defined time step. To use ML/DL for the task of classification, it is important to divide the images into different labels. As mentioned in the introduction, three labels for the classification task have been considered, namely, Safe, Critical, and TR, depending upon the maximum surface temperature of the battery. The extraction and partitioning of these images into various labels are made in such a way that each label contains the same or nearly the same number of images. This is due to the concept of a balanced dataset in ML. In any ML/DL problem, class imbalance [63] is a major problem, as it reduces the accuracy of the model, making the model biased towards the class having higher number of images. Further details on the image collection are provided in the results and discussion section. The next task is to preprocess the extracted data. Image preprocessing involves formatting the images before they can be used for training. This involves certain operations but is not limited to orienting, resizing, and color corrections. For the purpose of data preprocessing, techniques such as image normalization [64] and image augmentation [65] are used.

2.2.2. Thermal runaway classification using convolutional neural network (CNN)

Image classification [66] involves taking an input (a picture) and predicting a class label or a probability referring to the input is of a particular class. Convolutional neural networks have taken a quantum leap in image recognition. Additional information regarding CNNs has been provided in the SI. In this work, CNNs are used to classify three labels, i.e., safe, critical, and TR, which are directly related to the physical problem.

Learning takes place through an iterative process known as training. There are two methods by which training can be performed. The first method is learning from scratch. Learning from scratch is building completely a new model or mixing parts of other models and performing the training from the first layer. The second method is transfer learning with fine-tuning. This method consists of applying a pre-trained DL model to a dataset of interest. Transfer learning helps users to overcome the need for huge amounts of new data. A model already trained on a particular task will be able to manage a new but similar task with minimal data. Additionally, the process of training can be boosted by utilizing a pre-trained model. This can result in a more effective model. Transfer learning yields the best results when the datasets are similar to the one that the model was already pretrained. For completely different datasets, learning from scratch is preferable. Hence, in this study, training from scratch is performed as the dataset is unique compared to other large datasets used to pre-train models.

The CNN architectures employed in this study, including VGG16, VGG19, ResNet18, ResNet34, ResNet50, ResNet101, DenseNet121, DenseNet201, EfficientNetB6, EfficientNetB7, and MobileNetV3, are pre-established models widely recognized in the field of computer vision [67–69]. VGG16 and VGG19 are 16- and 19-layer CNN architectures, respectively, widely employed in visual object recognition software research. Both networks process RGB images as input, featuring a sequential stack of convolutional layers with small receptive fields and max-pooling layers [70]. ResNet, or Residual Network, variants used in this study include ResNet18, ResNet34, ResNet50, and ResNet101. These architectures leverage the concept of residual learning, incorporating residual connections to facilitate the training of deeper networks [71]. The increased depth enables superior performance across various classification tasks. DenseNet121 and DenseNet201 are DenseNet architectures, where each layer receives input from all preceding layers [72]. Dense connectivity patterns contribute to efficient parameter usage, addressing vanishing gradient issues and enhancing overall model performance. The EfficientNet family includes EfficientNetB6 and EfficientNetB7, offering efficient scaling of depth, width, and resolution to achieve a balance between model size and accuracy [69]. These networks are particularly well-suited for resource-constrained environments. MobileNetV3 is part of the MobileNet family, designed for efficient deployment on mobile and edge devices [73]. It incorporates inverted residuals and linear bottlenecks for reduced computational cost, making it ideal for real-time applications. These models are well established, and details of their network architecture can be readily found elsewhere [69–73].

2.2.3. Object detection using YOLO

YOLO is an approach in the field of object detection using advanced DL algorithms. Here, object detection is performed as a regression problem, starting from the pixels of the image to the coordinates of the bounding box, to calculate the class probabilities [50]. Fig. 2 shows a schematic illustration of YOLO network architecture. In this work, YOLO version 5 has been utilized for the purpose of object detection. The YOLO architecture begins with an input layer that takes battery thermal images as the initial data for the subsequent layers of the network. The core of YOLO consists of a backbone network comprising twenty-four convolutional layers, which are responsible for extracting hierarchical features from the input image. As these layers progress, they capture increasingly abstract and complex representations, allowing the model

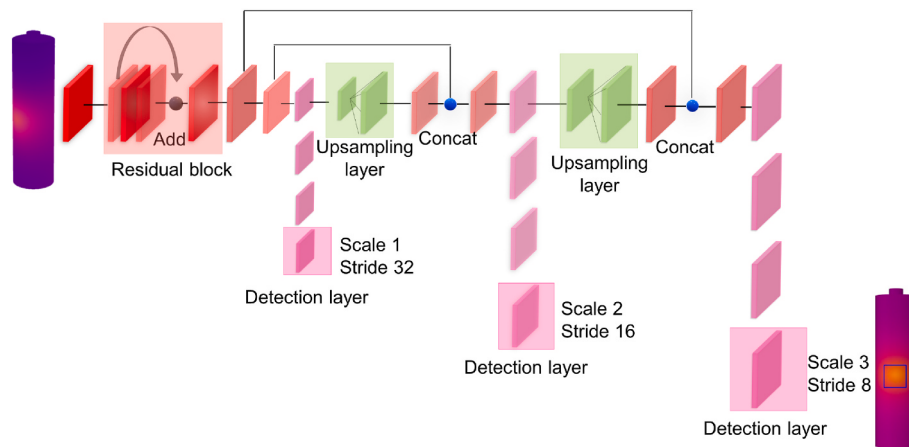


Fig. 2. A schematic illustration of the YOLO network architecture, together with the input image and its corresponding output available from the deep learning network.

to discern intricate patterns in the visual data. Following the convolutional layers, YOLO integrates two fully connected layers that further process the extracted features, enhancing the network's ability to understand and interpret the visual information. YOLO also incorporates 1x1 reduction layers strategically within the architecture. These layers serve to reduce the dimensionality of the feature maps, optimizing computational efficiency while preserving critical information. Subsequent to the reduction layers, YOLO employs 3x3 convolutional layers. These layers play a crucial role in capturing spatial dependencies within the feature maps, facilitating the model's understanding of the spatial relationships between different elements in the image. The final stage of the YOLO architecture is the output layer, which produces a $7 \times 7 \times 30$ tensor. This tensor represents the output of the detection layer of the network, with each cell in a 7×7 grid over the input image producing 30 predictions. Each prediction is a vector that contains the (x, y) coordinates of the center of a bounding box, the width and height of the bounding box, the confidence score (objectness score), and class probabilities for each of the classes the model is trained to recognize. These predictions are encoded in the form of a tensor, and the information can be extracted and used to identify and locate objects within the input image. In essence, the YOLO architecture is carefully designed, progressing through convolutional backbones, fully connected layers, 1x1 reduction layers, and 3x3 convolutional layers. The final tensor output, structured as $7 \times 7 \times 30$, efficiently encodes rich information for object localization and class predictions across the image grid. This detailed architecture empowers YOLO to excel in real-time and accurate object detection across a diverse range of datasets and scenarios.

3. Results and discussion

The primary objective of the present work is to predict thermal runaway in Li-ion batteries using combined multiphysics modeling and advanced ML/DL algorithms. The first part presents and discusses the multiphysics modeling results of Li-ion batteries under a different load. This is followed by the results obtained by applying DL techniques to the thermal images obtained from the multiphysics model.

3.1. Thermo-electrochemical model

It is challenging experimentally to observe the TR events in real time. Moreover, during the battery preparation and its thermal treatment, a variety of side reactions could be triggered [74]. All these features might potentially influence the propagation of the LIB's TR, causing some parts of the battery to be more susceptible to failures than others. Therefore, the exact modeling of the TR is not straightforward, considering the incomplete state of knowledge about the TR's associated events. For this

reason, in the current modeling work, the locations of the TR hotspots are randomly chosen for cases with one and two hotspots. The schematic of the model containing a single hotspot is shown in the supplementary information (cf. Fig. S3). First, the multiphysics modeling results with one hotspot are presented, followed by the results for two hotspots, with the details of the effect of degradation on battery temperature and the capacity fade.

The developed model is used to investigate the effect of cell degradation on the temperature and battery capacity. For the simulation, a constant current/constant voltage (CCCV) charging is considered. Since, the current at which the voltage was validated is extremely small to initiate significant degradation, the cell is discharged at a 1C rate until it reaches a cut-off voltage of 2.5 V, followed by charging to 4.2 V. However, the heat release during this operation of the battery is observed to be sluggish, and the temperature rise is not sufficient for SEI decomposition to occur. Following this observation, the cell is discharged and charged at a 2C rate. Fig. 3 shows the profile for charge and discharge curves pertaining to a single TR hotspot (cf. Fig. 3a), the change in the SEI thickness for one (red) and two (blue) TR hotspots, respectively (cf. Fig. 3b), and the rise in the maximum cell temperature of the battery for one (red) and two (blue) TR hotspots respectively (cf. Fig. 3c). Ideally, any battery needs large number of cycles to show prominent SEI growth, and the differences in the cycle to cycle behavior is usually assumed small. Hence, the SEI growth rate is accelerated by increasing the pre-exponential factor for proof of concept. This is a valid assumption for modeling purposes to observe the TR faster. Additionally, Fig. 3b illustrates the effect of the aging process on the growth of SEI formation. It is evident that the aging process slows down the rate of growth of SEI with time. This occurs as we have considered the SEI formation to be limited by a diffusion process through the formed SEI film.

Fig. 3 shows the reduction in the SEI thickness during discharge, implying the SEI decomposition reaction. As expected, a comparison between the temporal variations of the temperature in Fig. 3c indicates a more rapid temperature rise for the system with two TR hotspots. It should be mentioned that the model terminates after the stop condition is satisfied at 400 K, hence, the SEI does not completely decompose, as illustrated in Fig. 3b. SEI decomposition releases heat and increases the temperature of the battery. The exponential trend of the temperature evolution, as seen in Fig. 3c is explained by the Arrhenius relation of the SEI decomposition heat release [28]. This trend in the rise of temperature due to the degradation of the battery has been well reported in prior literature. Additionally, it was observed that the electrochemical HGR (cf. Eq. 7) was significantly lower in comparison to the heat release due to the degradation (SEI decomposition). Hanchard et al. [33] have devised a 1D model to estimate the variation of temperature during the TR event of LCO/graphite cells placed in a constant temperature oven

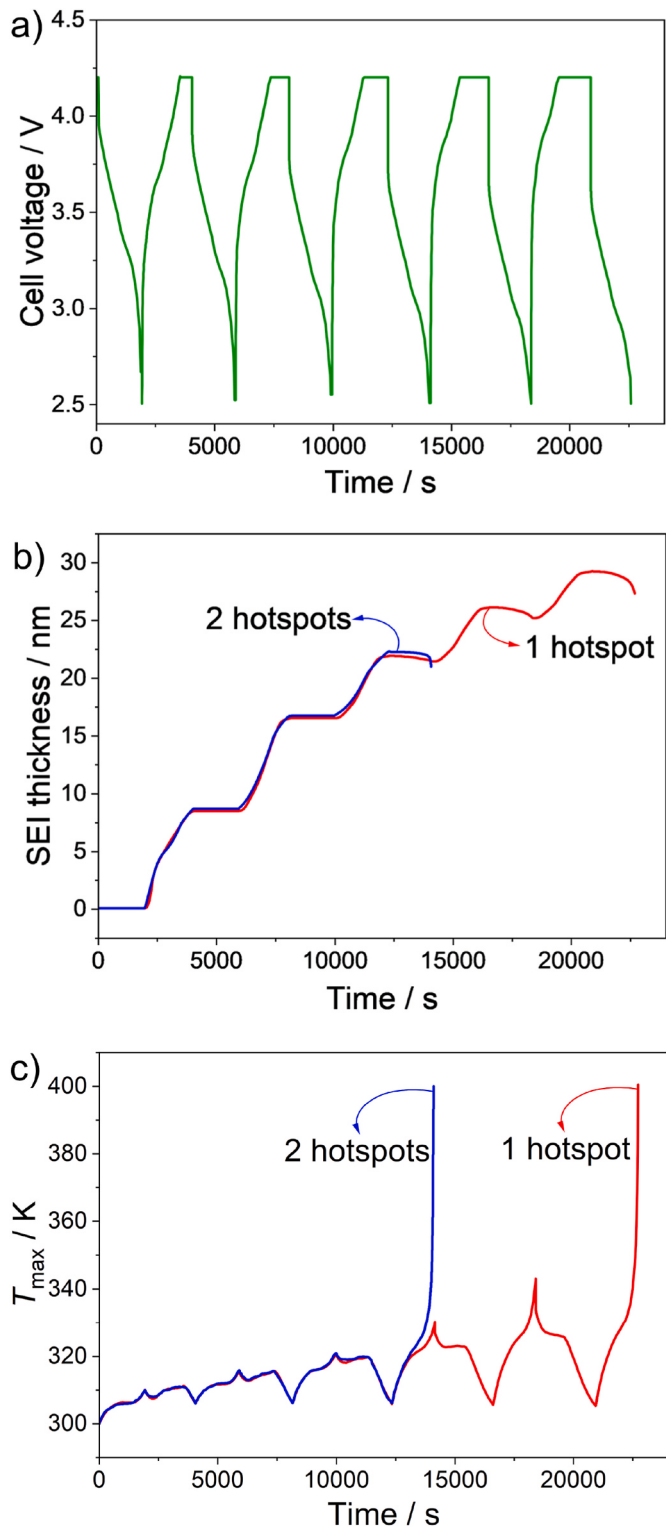


Fig. 3. Multiphysics modeling results illustrating the variation of general parameters relating to the electrochemical-thermal model with respect to time. (a) Charge/discharge curves for one TR hotspot; (b) SEI thickness change for one (red) and two (blue) hotspots; and (c) Maximum temperature for the 18650 Li-ion battery. (For interpretation of the references to color in this figure legend, the reader is referred to the Web version of this article.)

during discharge and report similar temporal temperature profiles as in the results presented in this work(cf. Fig. 3). Kim et al. [27] have performed thermal abuse tests based on a 3D lumped model for the TR prompted by heating. The authors have reported the evolution of temperature to follow an exponential trend that is similar to the results shown in Fig. 3c. The introduction of hotspots would induce non-uniform temperature distribution inside the battery and, thus, non-uniform SEI generation. However, the SEI growth process has been implemented in the P2D model that assumes a uniform SEI growth for the negative electrode. The study of non-uniform SEI generation requires a 3D particle model in addition to a full-scale battery model and is subject to future work.

Fig. 4 illustrates the total heat generation rate of the battery during operations for single (red) and two (blue) TR hotspots. At the beginning, both curves follow the same trend corresponding to the charge/discharge cycling. During the discharge, exothermic processes dominate, leading to the heat release, while the charging process is endothermic in nature, causing some heat to be absorbed by the battery. The exponential heat generation rate is due to the SEI decomposition reaction, which leads the battery to the TR. The model containing a single hotspot contains a single Arrhenius function applied at that location, indicating the heat release due to the degradation of the battery, whereas the model with two hotspots contains two Arrhenius functions acting at the locations individually. Due to this reason, the sudden exponential heat release is observed sooner for the model with two hotspots as compared to the one with a single hotspot. A similar trend of heat release leading to the TR has been reported by Feng et al. [18] through experimental and modeling studies.

The capacity fade can be observed in the discharge curves of graphite/NMC cell through operation for 2C charge/discharge as shown in Fig. 5. The first discharge curve obtained from the simulations was directly compared to the datasheet provided by the battery manufacturer. It was observed that these results are in good agreement with the experimental test results [75]. Specifically, experimentally the open circuit voltage of 4.2 V, along with the cut-off voltage of 2.5 V agrees well with the modeling results reported in Fig. 5. Further details about the specifications of the battery are provided in the supplementary information. During the battery operation, the main contribution to the capacity fade is due to the cyclable loss of lithium induced by the SEI formation. A shift is observed in the voltage curve at the end of the discharge. Additionally, as the number of cycles increases, the capacity

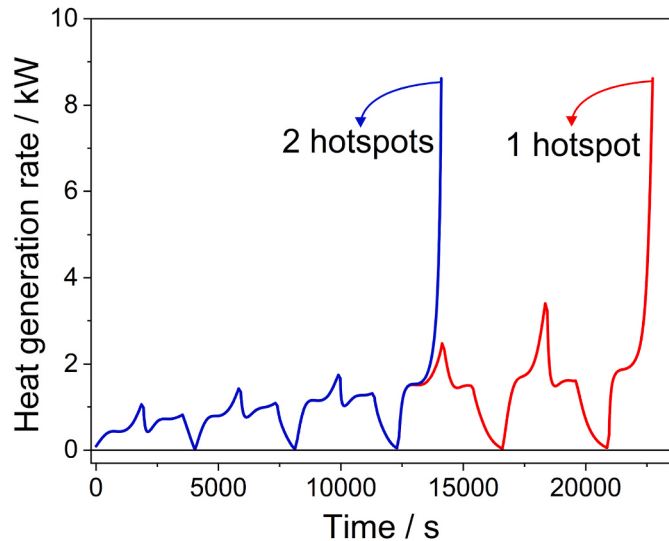


Fig. 4. Comparison of heat generation rates during the battery operation for the model with one hotspot (red) and two hotspots (blue). (For interpretation of the references to color in this figure legend, the reader is referred to the Web version of this article.)

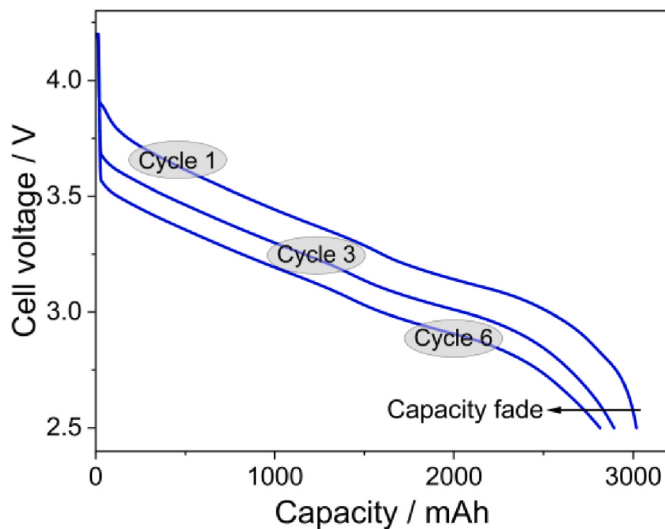


Fig. 5. Multiphysics simulation results for the cell voltage vs. the capacity of the cell in operation involving degradation of the battery, showing results for three discharge cycles (cycle 1, cycle 3, and cycle 6).

tends to decrease, and the cut-off voltage is reached earlier.

This SEI formation-induced capacity fade has also been observed in experiments [76]. Ramadass et al. [77] and Lin et al. [78] have studied the degradation of different Li-ion cells, and observed a shift in voltage. Additionally, they have reported that an SEI layer is formed on the surface of the negative electrode. The passive layer reduces the amount of cyclable lithium that leads to capacity fade with a shift in the

potential. Accurate modeling of the TR is a challenging task. The objective during the model construction has been to extract thermal images of the battery, which provide a qualitative aspect of the TR initiation. The goal is to predict TR using ML on the thermal images extracted from simulations. The introduction of hotspots artificially within the battery for the initiation of the TR has already been mentioned. There could be multiple hotspots inside the battery depending upon the degradation mechanisms. The locations of these hotspots are completely random. For this study, the number and locations of the hotspots has been varied within the battery to investigate the evolution of the cell temperature. Fig. 6a shows the view of a battery for a constant 2C charge/discharge current with airflow velocity at the inlet being 0.1 m s^{-1} . The general schematic of the computational domain, along with the respective boundary conditions, is provided in the supplementary information (Fig. S3). It can be observed that due to the heat release from the SEI decomposition at the hotspot location, causes the temperature of the entire battery to rise and eventually lead to the TR. Fig. 6b-d shows the results for the battery temperature with cooling airflow for two high-temperature hotspots at different locations within the battery and the location is given with respect to the height of the battery (h_{batt}) and the radius of the battery (r_{batt}). Due to the heat release from the SEI decomposition reaction, other exothermic reactions are triggered, and this increases the temperature of the entire battery, triggering the TR event. Additionally, we observe distinct thermal behaviors when comparing scenarios with one versus two hotspots. The presence of two hotspots accelerates the thermal gradient development within the cell, underscoring a nonlinear escalation in risk factors leading to TR. This phenomenon is particularly evident in the rate of temperature rise (cf. Fig. 5c) and the spatial temperature distribution (cf. Fig. 6b-d). Our analysis provides crucial insights into the interplay of hotspot number and location, offering a comprehensive

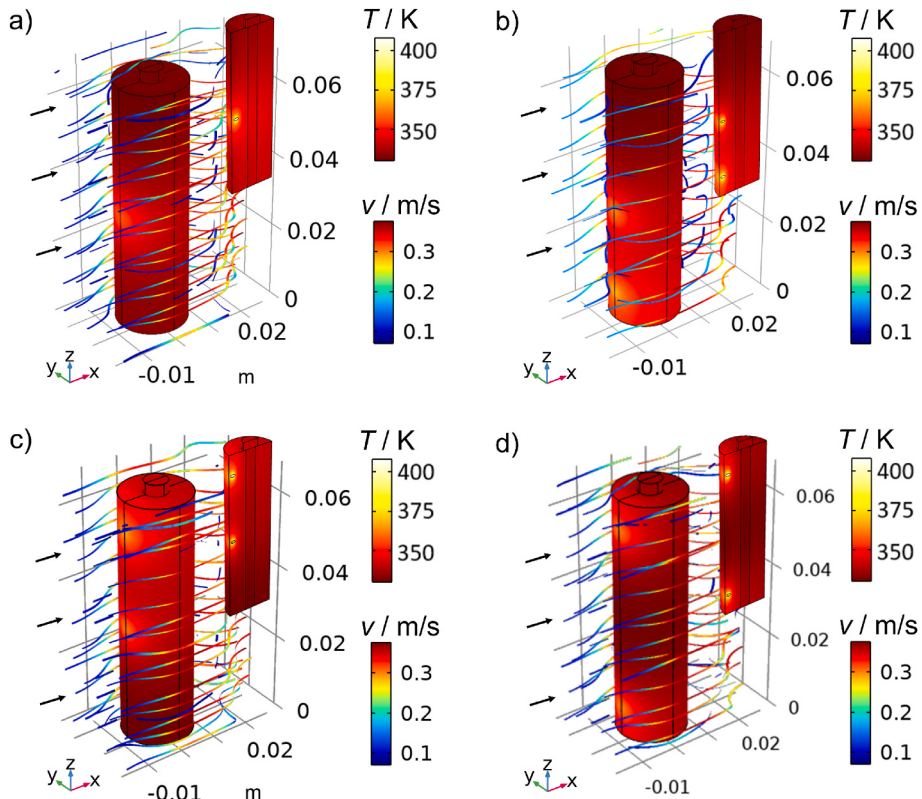


Fig. 6. Temperature distribution of the battery surface along with air cooling for single and two hotspots at 2C charge/discharge rate. a) Single hotspot, b) two hotspots at $\frac{h_{\text{batt}}}{6}$ mm and $\frac{h_{\text{batt}}}{2}$ mm from the bottom, c) two hotspots at $\frac{h_{\text{batt}}}{2}$ mm and $\frac{5h_{\text{batt}}}{6}$ mm from the bottom, and d) two hotspots at $\frac{h_{\text{batt}}}{6}$ mm and $\frac{5h_{\text{batt}}}{6}$ mm from the bottom. All hotspots are a distance of $\frac{3h_{\text{batt}}}{2}$ from the center of the battery in the radial direction. The figure shows the temperature of the battery and streamlines only represent the velocity magnitude of the cooling fluid. The velocity at the surface of the battery is zero due to the no-slip condition.

understanding of their impact on cell safety and performance.

3.2. Deep learning results

DL enables a significantly broader scope of the study of LIBs. Many ML methods have been shown to be extremely promising in the study of material properties in LIBs and the estimation of the state-of-charge (SOC) of a battery [38]. Due to these efficient applications, DL has received significant attention in recent years. Predicting TR events in batteries using DL is a relatively new approach. There are very few works in the prior literature that use the idea of data-driven DL to forecast such events. Based on a thorough search of relevant literature, there is no work that uses an image-driven DL approach to forecast TR events, which is one of the novel aspects of this work. The multiphysics modeling results are taken as input to different DL techniques to identify and predict the TR. This section is divided into two parts. First, the results for the TR prediction as a classification task based on different DL architectures has been reported. Finally, the object detection technique, based on a regression approach, has been utilized to detect the high-temperature hotspots created within the battery at random locations due to the degradation mechanism.

3.2.1. Thermal runaway classification

The TR classification requires the use of DL algorithms that learns to assign a class label to test data from the problem domain. To perform the task of classification, data preparation, and preprocessing is the most important step. For the data preparation step, images were collected and specified under a particular label based on the maximum temperature of the battery. When the maximum surface temperature is below 340 K, the images belong to the Safe class. The Critical class is defined when the maximum surface temperature is between 340 K and 370 K, also called the transition stage between the Safe and the TR regions. Finally, for temperatures greater than 370 K [79], the images are considered to belong in the TR class. To ensure an equal number of images for each label, the time at which the images were extracted from the multiphysics model played a vital role. During the simulation, the maximum battery temperature tends to be lower than 340 K for a long period of time due to the normal operation for the initial cycles, hence for this case, the time step is 100 s. For the transition phase between the safe and the TR region, i.e., the critical stage, the time step size is taken to be 10 s due to the process being fast. Finally, for the TR stage, which happens rapidly, the time step size is taken to be 1 s, ensuring an equal number of images extracted for each class of the DL model. This resulted in the collection of 1200 images, with each class having 400 images, respectively. This is the size of the entire dataset. The next step is the data preprocessing, where the images are preprocessed using various techniques that have been discussed in the methodology section. Following this partitioning, the next task involved the splitting of the data into training, validation, and test sets, where the training set is fed as input to the model, and the validation set is used to evaluate the performance of the model during training. The training set contained 80 % of the total number of images in the entire dataset, whereas the validation and the test sets contained 10 %, respectively.

The performance of the DL model is assessed through the learning curves obtained from the training data. This is provided in the supplementary file. The training is performed over 300 epochs for each of the networks used. Additionally, a study was performed to observe the effect of different hyperparameters on the overall model accuracy using all the networks individually. For this purpose, batch size, optimizer, and the learning rate were chosen to be varied and optimized. Batch size [80] is one of the most important hyperparameters to tune in modern DL systems. Larger batch size is mostly preferred as this gives the model the opportunity to look at larger data at any instant of training. The downside of a higher batch size is its high computational memory usage and higher training time. In this study, the batch size is varied as 8, 16, 32, and 64 and training is performed for the same number of epochs.

Comparing the accuracies for batch sizes of 32 and 64 gives the best results for all the networks taken into consideration, with the latter giving a slightly higher accuracy at the cost of much higher training time and memory usage. For this reason, a batch size of 32 was chosen. After optimizing batch size, the next important hyperparameter, i.e., the learning rate, was varied. In ML, the learning rate stands as a configurable parameter within optimization algorithms [81]. It plays a pivotal role in dictating the size of each step taken during iterations as the algorithm progresses towards minimizing a loss function. Symbolizing the degree to which recently acquired information supersedes prior knowledge, the learning rate serves as a metaphorical indicator of the swiftness with which an ML model assimilates new insights. Hence, optimizing the learning rate becomes very crucial. For this study, the learning rate was varied across different values of 0.01, 0.001, 0.0001, and 0.00001. The learning rate of 0.00001 yielded a slightly higher accuracy compared to 0.0001 at the cost of significantly longer training times. Therefore, a learning rate of 0.0001 was selected as the final value. Following the optimization of the batch size and the learning rate, the choice of optimizer was varied. Optimizers refer to algorithms or techniques employed to diminish the loss function or enhance production efficiency. These mathematical functions are contingent upon the learnable parameters of a model, namely the weights. Optimizers play a crucial role in determining the adjustments to the weights and learning rate of a neural network, aiding in the reduction of losses. Three popular optimizers – Stochastic Gradient Descent (SGD), Adam, and RMSprop – were considered for the purpose of optimizer tuning [82]. It was revealed that the Adam optimizer delivered the best results, and thus, it was selected as the final optimizer. Following the tuning of hyperparameters, then the optimized models were trained and tested on the test dataset. Estimation of the essential statistical parameters is necessary for assessing the performance of the model for the classification task. These parameters have already been described in the methodology section. The complete list of values for accuracy, precision, recall, and F1 score is reported in Table 1. Upon analyzing the results presented in Tables 1 and it becomes evident that EfficientNetB7 outperforms its counterparts in terms of accuracy, recall, and F1 score. This finding signifies the superior efficacy of EfficientNetB7 in accurately predicting the class labels of images within the test dataset. Notably, the recall value for EfficientNetB7 stands out as notably higher compared to other networks, a critical aspect given its implication for safety considerations. A high recall value indicates a more precise identification of positive instances, a paramount factor in scenarios where misclassifying images with the TR label could lead to disastrous outcomes. The commendable performance of EfficientNetB7, as indicated by the elevated values of these performance metrics, suggests its potential extension to images derived from experimental data. Moreover, the high values of the performance metrics indicate that this idea can also be well extended to images collected from experimental data and could significantly help in predicting real-time TR detection in batteries.

Fig. 7 shows the confusion matrices for the best model for each group

Table 1

Performance of the networks used in this study based on the most important performance metrics.

Deep learning architecture	Accuracy	Precision	Recall	F1-score
VGG16	0.96	0.89	0.88	0.95
VGG19	0.96	0.98	0.87	0.96
ResNet18	0.91	0.88	0.91	0.89
ResNet34	0.95	0.92	0.93	0.95
ResNet50	0.98	0.95	0.95	0.97
ResNet101	0.98	0.96	0.97	0.97
DesneNet121	0.95	0.91	0.93	0.92
DenseNet201	0.96	0.93	0.95	0.96
EfficientNetB6	0.99	0.94	0.96	0.97
EfficientNetB7	0.99	0.97	0.98	0.96
MobileNetV3	0.93	0.90	0.91	0.90

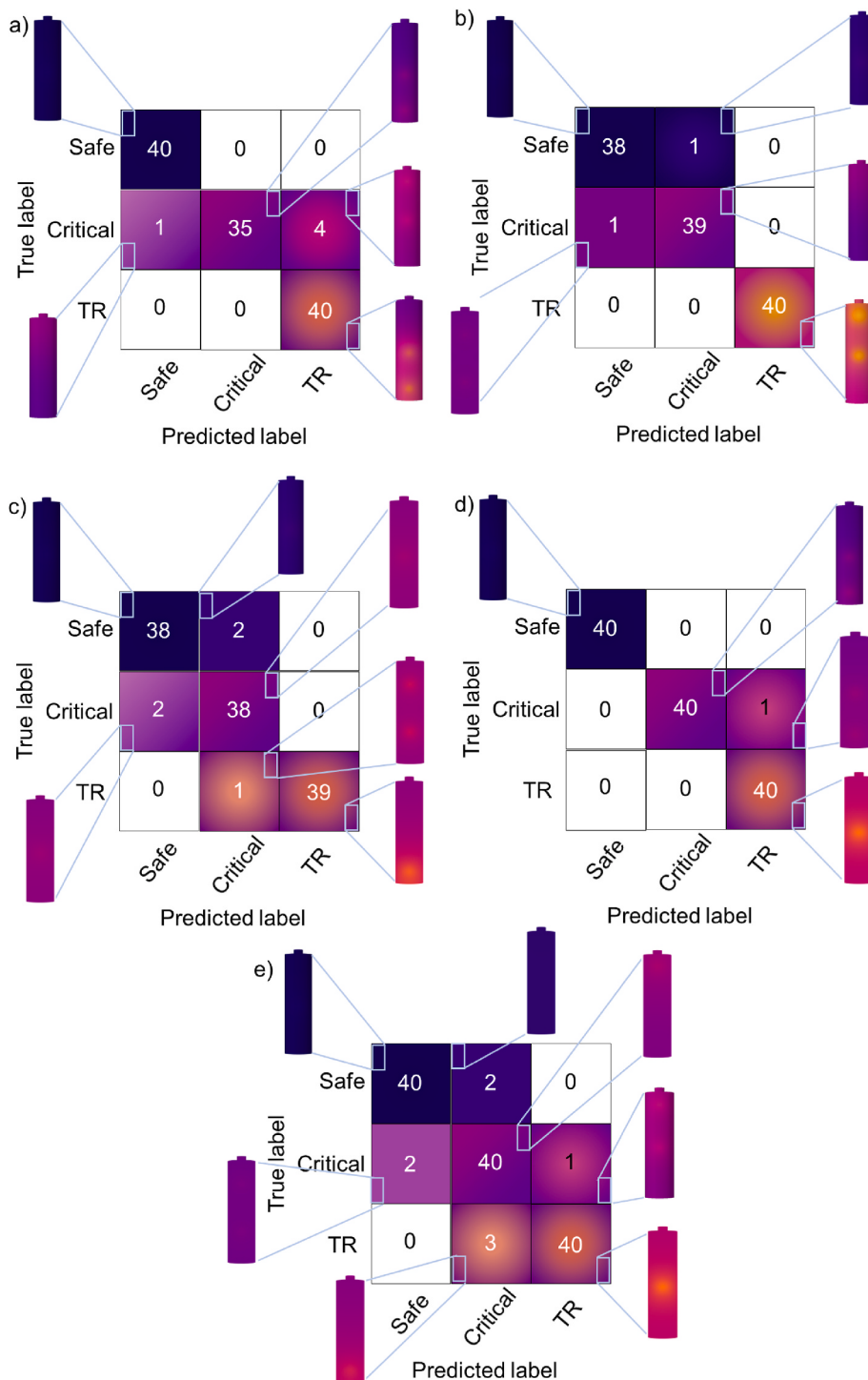


Fig. 7. Confusion matrix on the test dataset for different types of networks trained along with visualization of the images predicted for each label and their corresponding misclassifications: (a) VGG19, (b) ResNet101, (c) DenseNet201, (d) EfficientNetB7, and (e) MobileNetV3.

of networks considered in this paper. For instance, among the VGG group, the confusion matrix for VGG19 has been reported. Using a similar idea, confusion matrices of ResNet101, DenseNet201, EfficientNetB7, and MobileNetV3 are reported. This approach would provide qualitative and quantitative insights about the performance and robustness of different types of network to the given problem rather than just comparing between the same type of networks with different layers. Since this is a three-label classification problem, the matrices are 3×3 in dimension. Here, the diagonal elements represent the number of images that are rightly classified according to their true labels. The off-

diagonal elements represent the number of misclassifications for each label. Considering the first confusion matrix for VGG19, as shown in Fig. 7a, there are a total of 5 miss-classifications, all belonging to the same label. Among the 40 images, 35 of them are correctly classified, and among the five misclassifications, one image is misclassified as safe, and the other four images are misclassified as TR. Fig. 7b shows the confusion matrix for ResNet101. There are only two misclassifications for this network. Here, one image is misclassified as Critical while being in Safe, and the other one as Safe while being in Critical. Fig. 7c shows the confusion matrix for DenseNet201, having 5 misclassifications out of

120 images in total. 2 images in the Safe label are misclassified as Critical, and another 2 images in the Critical label are misclassified as Safe. Similarly, Fig. 7d shows the confusion matrix for EfficientNetB7, having no misclassifications. As the name goes, it is indeed the most efficient model for this problem. Finally, Fig. 7e shows the confusion matrix for MobileNetV3, showing the most number of misclassifications among the other models and it is also evident from Table 1 that reports the least accuracy for this model. Additionally, Fig. 7 shows a glimpse of the images for each of the cells in the confusion matrix, which provides a better visual representation and qualitative insight into the results obtained. Overall, it can be concluded that EfficientNetB7 performs the best among all the used DL methodologies.

All three models exhibit good performances in predicting the labels accurately with minimal numbers of miss-classifications, which are acceptable from a statistical point of view. The test set is an unknown set, meaning the model has not previously seen it. A good performance on an unknown set signifies that the model is robust and has a good generalizing ability. The incorporation of scenarios with varying hotspot numbers significantly enhances the predictive robustness of our CNN models. The comparative analysis between single and dual hotspot situations reveals a marked improvement in the model's ability to discern complex thermal patterns, a key factor in predicting TR. This enhancement is quantified through improved accuracy and recall metrics in our models, indicating their heightened sensitivity to subtle variations in thermal imagery. These findings underscore the critical role of diverse training datasets in developing reliable predictive models for battery safety applications. Although the developed ML framework shows outstanding results in predicting thermal failures with great accuracy based on a single thermal image, there are certain challenges to extend it to a real battery module/pack due to its packaging, housing, etc. The results indicate the possibility for the application of various ML techniques to different views of a single cell and accurately predicting thermal failures. This approach can be well extended to the battery pack/module for effective prediction of thermal failures. It should be noted that using CNN with images for this study can sometimes lead to 'fake warnings'. However, to mitigate this risk, a detailed multiphysics model has been developed in this work, including SEI degradation to initiate TR. This model simulates realistic thermal images of batteries, providing diverse and realistic data for training various CNN architectures. Emphasizing rigorous training on a well-curated dataset, including multiple hotspots, further enhances CNN's understanding of thermal behavior. Additionally, the methodology incorporates robust data preprocessing, rigorous validation, and hyperparameter tuning during the CNN training process. This multifaceted approach not only improves the CNNs' predictive capabilities but also ensures their reliability in practical applications.

3.2.2. Object detection

Object detection is a technique in the field of computer vision that helps to identify and track objects in a video or image [83]. Object detection can be utilized for effectively counting objects in a scene and determining their precise locations, along with accurately labeling them. In this paper, this technique to predict TR events in LIBs is applied. Fig. 8 shows some predictions (output of network) of YOLO on different thermal images of batteries obtained from the multiphysics model simulations. In Fig. 8, three different images of the battery are shown as the test data for input. These images contain single and double high-temperature hotspots at different locations. The results indicate the high efficiency of YOLO in predicting the regions of TR initiation/hotspots where the temperature is very high compared to the other regions of the battery. This idea can also be extended for real-time TR hotspot detection in experimental battery operation.

4. Conclusion

A combined multiphysics model and DL-based framework has been

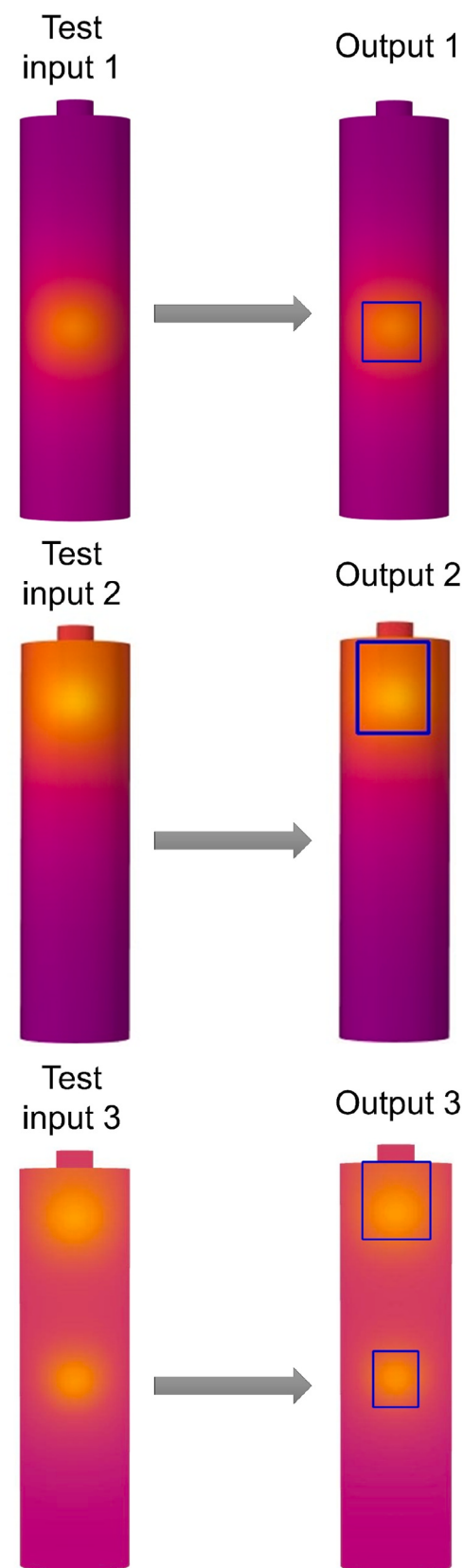


Fig. 8. Results for object detection technique showing different thermal images of the battery as input and its corresponding output containing bounding boxes over the high-temperature hotspots.

developed for predicting the TR in cylindrical Li-ion batteries. This paper contributes to the prevention of unfortunate events of the explosion of the battery operating devices (e.g., cell phones, EVs) in terms of both practical advances and improved fundamental understanding. The multiphysics model utilizes the COMSOL software to simulate the electrochemical-thermal nature of cylindrical battery type at various conditions. The thermal images of the battery obtained from the simulations are preprocessed for application in DL.

The ML/DL study is divided into two parts. First, a classification technique is used, which involves using CNNs for real-time prediction of the TR in the battery. Then, the YOLO (an object detection technique) is implemented and applied to the battery thermal images for the detection of the high-temperature hotspot zones. The performances of the DL classification algorithms and the object detection technique show great performance in the classification of the TR and predicting the location of the hotspots in the battery well. In the context of benchmarking thermal runaway classification, this study emphasizes the selection of maximum temperature as a primary criterion, reflecting its direct correlation with critical conditions leading to thermal runaway. The choice is grounded in the practical significance of maximum temperature as a clear and straightforward indicator of peak thermal stress experienced by the battery. This parameter provides a tangible and easily interpretable benchmark for distinguishing safe, critical, and thermal runaway states, aligning with the overarching objective of predicting and preventing thermal runaway in cylindrical Li-ion batteries. While acknowledging the importance of temperature rising rates in understanding thermal dynamics, prioritizing maximum temperature offers a pragmatic and actionable approach for assessing battery safety.

The developed framework can be extended for real-time TR hotspot detection and for practical battery operation. The main advantage of the proposed DL techniques is that they do not require the physical modeling of the internal battery chemistry, which is cumbersome in the TR scenario, rather, they rely only on the experimental/modeling data and the collected thermal images.

There are certain practical challenges associated with acquiring thermal images in real-world scenarios. However, the decision to incorporate thermal images as inputs for the ML modeling is based on their unique advantages, providing a comprehensive representation of spatial and temporal temperature variations within the battery. This approach enables early detection of potential issues and seamless integration with the multiphysics modeling methodology. While recognizing concerns about data storage, we argue that the benefits in predictive accuracy and safety outcomes justify the use of thermal images. With advancing technology facilitating the handling of large datasets, including thermal imaging data, making it increasingly practical to handle large datasets. Although this method of predicting battery failures seems a viable option towards ensuring the safety of electric vehicles, there are a few potential limitations in its practical implementation on a large scale. Firstly, the initial cost to setup might be significantly high. Secondly, the various types of degradation that are possible, along with more cell designs, should be considered as well. This would help in creating a larger dataset that would be more reliable than the present one. It must be noted that the developed multiphysics modeling and ML framework is generic and may be well extended to various Lithium-ion batteries with various geometric configurations and contrasting anode/cathode materials in addition to cylindrical cells.

CRediT authorship contribution statement

Basab Ranjan Das Goswami: Data curation, Formal analysis, Investigation, Methodology, Visualization, Writing – original draft, Writing – review & editing. **Massimiliano Mastrogiovio:** Formal analysis, Investigation, Writing – original draft, Writing – review & editing. **Marco Ragone:** Conceptualization, Formal analysis, Investigation, Methodology, Writing – original draft, Writing – review & editing. **Vahid Jabbari:** Formal analysis, Writing – original draft,

Writing – review & editing. **Reza Shahbazian-Yassar:** Formal analysis, Writing – original draft, Writing – review & editing. **Farzad Mashayek:** Formal analysis, Writing – original draft, Writing – review & editing. **Vitaliy Yurkiv:** Conceptualization, Funding acquisition, Investigation, Methodology, Resources, Supervision, Writing – original draft, Writing – review & editing.

Declaration of competing interest

The authors declare that they have no known competing financial interests or personal relationships that could have appeared to influence the work reported in this paper.

Data availability

Data will be made available on request.

Acknowledgments

The authors acknowledge the financial support from the National Science Foundation (Award CBET-2313395).

Appendix A. Supplementary data

Supplementary data to this article can be found online at <https://doi.org/10.1016/j.jpowsour.2024.234065>.

References

- [1] K. Edström, R. Dominko, M. Fichtner, T. Otuszewski, S. Perraud, C. Punckt, J. Tarascon, T. Vegge, W. Martin, BATTERY 2030+ Roadmap, 2020, p. 83.
- [2] B.R. Das Goswami, V. Jabbari, R. Shahbazian-Yassar, F. Mashayek, V. Yurkiv, Unraveling ion diffusion pathways and energetics in polycrystalline SEI of lithium-based batteries: combined cryo-HRTEM and DFT study, *J. Phys. Chem. C* 127 (2023) 21971–21979, <https://doi.org/10.1021/acs.jpcc.3c05395>.
- [3] V. Yurkiv, V. Jabbari, M. Mastrogiovio, B.R. Das Goswami, M. Ragone, R. Shahbazian-Yassar, F. Mashayek, Revealing the structure and properties of polycrystalline components of the solid electrolyte interface, *ECS Meet. Abstr. MA2022-01* (2022) 251, <https://doi.org/10.1149/MA2022-012251mtgabs>, 251.
- [4] J.B. Goodenough, K.S. Park, The Li-ion rechargeable battery: a perspective, *J. Am. Chem. Soc.* 135 (2013) 1167–1176, <https://doi.org/10.1021/ja3091438>.
- [5] S. Hwang, S.M. Kim, S.M. Bak, S.Y. Kim, B.W. Cho, K.Y. Chung, J.Y. Lee, E.A. Stach, W. Chang, Using real-time electron microscopy to explore the effects of transition-metal composition on the local thermal stability in charged $\text{Li}_{x}\text{Ni}_{y}\text{Mn}_{z}\text{Co}_{1-y-z}O_2$ cathode materials, *Chem. Mater.* 27 (2015) 3927–3935, <https://doi.org/10.1021/acs.chemmater.5b00709>.
- [6] P. Sun, R. Bisschop, H. Niu, X. Huang, A review of battery fires in electric vehicles, *Fire Technol.* 56 (2020) 1361–1410, <https://doi.org/10.1007/s10694-019-00944-3>.
- [7] C. Hendricks, N. Williard, S. Mathew, M. Pecht, A failure modes, mechanisms, and effects analysis (FMMEA) of lithium-ion batteries, *J. Power Sources* 297 (2015) 113–120, <https://doi.org/10.1016/j.jpowsour.2015.07.100>.
- [8] G.E. Blomgren, The development and future of lithium ion batteries, *J. Electrochem. Soc.* 164 (2017) A5019–A5025, <https://doi.org/10.1149/2.0251701jes>.
- [9] S. Abada, G. Marlair, A. Lecocq, M. Petit, V. Sauvant-Moynot, F. Huet, Safety focused modeling of lithium-ion batteries: a review, *J. Power Sources* 306 (2016) 178–192, <https://doi.org/10.1016/j.jpowsour.2015.11.100>.
- [10] Q. Wang, P. Ping, X. Zhao, G. Chu, J. Sun, C. Chen, Thermal runaway caused fire and explosion of lithium ion battery, *J. Power Sources* 208 (2012) 210–224, <https://doi.org/10.1016/j.jpowsour.2012.02.038>.
- [11] X. Feng, M. Ouyang, X. Liu, L. Lu, Y. Xia, X. He, Thermal runaway mechanism of lithium ion battery for electric vehicles: a review, *Energy Storage Mater.* 10 (2018) 246–267, <https://doi.org/10.1016/j.ensm.2017.05.013>.
- [12] X. Feng, X. He, M. Ouyang, L. Wang, L. Lu, D. Ren, S. Santhanagopalan, A coupled electrochemical-thermal failure model for predicting the thermal runaway behavior of lithium-ion batteries, *J. Electrochem. Soc.* 165 (2018) A3748–A3765, <https://doi.org/10.1149/2.0311816jes>.
- [13] H. Maleki, J.N. Howard, Internal short circuit in Li-ion cells, *J. Power Sources* 191 (2009) 568–574, <https://doi.org/10.1016/j.jpowsour.2009.02.070>.
- [14] B.R. Das Goswami, M. Mastrogiovio, M. Ragone, F. Mashayek, V. Yurkiv, A combined multiphysics modelling and machine learning to predict electro-thermal failures of cylindrical Li-ion batteries, *ECS Meet. Abstr. MA2022-01* (2022) 190, <https://doi.org/10.1149/MA2022-012190mtgabs>, 190.
- [15] M. Mastrogiovio, B.R. Das Goswami, M. Ragone, F. Mashayek, V. Yurkiv, Advanced data-driven modeling framework for predicting thermal failures in Li-ion

- pouch batteries, *ECS Meet. Abstr.* MA2022–01 (2022) 434, <https://doi.org/10.1149/MA2022-012434mtgabs>, 434.
- [16] B.R. Das Goswami, M. Mastrogiorgio, M. Ragone, F. Mashayek, V. Yurkiv, Predicting thermal failures using an advanced data-driven modeling framework in a cylindrical Li-ion battery pack, *ECS Meet. Abstr.* MA2022–02 (2022) 230, <https://doi.org/10.1149/MA2022-023230mtgabs>, 230.
- [17] Q. Wang, B. Mao, S.I. Stoliarov, J. Sun, A review of lithium ion battery failure mechanisms and fire prevention strategies, *Prog. Energy Combust. Sci.* 73 (2019) 95–131, <https://doi.org/10.1016/j.pecs.2019.03.002>.
- [18] X. Feng, S. Zheng, D. Ren, X. He, L. Wang, H. Cui, X. Liu, C. Jin, F. Zhang, C. Xu, H. Hsu, S. Gao, T. Chen, Y. Li, T. Wang, H. Wang, M. Li, M. Ouyang, Investigating the thermal runaway mechanisms of lithium-ion batteries based on thermal analysis database, *Appl. Energy* 246 (2019) 53–64, <https://doi.org/10.1016/j.apenergy.2019.04.009>.
- [19] P.T. Coman, E.C. Darcy, C.T. Veje, R.E. White, Modelling Li-ion cell thermal runaway triggered by an internal short circuit device using an efficiency factor and Arrhenius formulations, *J. Electrochem. Soc.* 164 (2017) A587–A593, <https://doi.org/10.1149/2.0341704jes>.
- [20] P. Coman, E. Darcy, R. White, Simplified thermal runaway model for assisting the design of a novel safe Li-ion battery pack, *J. Electrochem. Soc.* (2022), <https://doi.org/10.1149/1945-7111/ac62bd>.
- [21] D. Mishra, K. Shah, A. Jain, Investigation of the impact of flow of vented gas on propagation of thermal runaway in a Li-ion battery pack, *J. Electrochem. Soc.* 168 (2021) 060555, <https://doi.org/10.1149/1945-7111/ac0a20>.
- [22] Q. Wang, J. Sun, X. Yao, C. Chen, Thermal behavior of lithiated graphite with electrolyte in lithium-ion batteries, *J. Electrochem. Soc.* 153 (2006) A329, <https://doi.org/10.1149/1.2139955>.
- [23] D. Patel, J.B. Robinson, S. Ball, D.J.L. Brett, P.R. Shearing, Thermal runaway of a Li-ion battery studied by combined ARC and multi-length scale X-ray CT, *J. Electrochem. Soc.* 167 (2020) 090511, <https://doi.org/10.1149/1945-7111/ab7fb6>.
- [24] M.N. Richard, J.R. Dahn, Accelerating rate calorimetry study on the thermal stability of lithium intercalated graphite in electrolyte. II. Modeling the results and predicting differential scanning calorimeter curves, *J. Electrochem. Soc.* 146 (1999) 2078–2084, <https://doi.org/10.1149/1.1391894>.
- [25] M.N. Richard, J.R. Dahn, Accelerating rate calorimetry studies of the effect of binder type on the thermal stability of a lithiated mesocarbon microbead material in electrolyte, *J. Power Sources* 83 (1999) 71–74, [https://doi.org/10.1016/S0378-7753\(99\)00260-8](https://doi.org/10.1016/S0378-7753(99)00260-8).
- [26] M.N. Richard, J.R. Dahn, Accelerating rate calorimetry study on the thermal stability of lithium intercalated graphite in electrolyte. I. Experimental, *J. Electrochem. Soc.* 146 (1999) 2068–2077, <https://doi.org/10.1149/1.1391893>.
- [27] G.H. Kim, A. Pesaran, R. Spotnitz, A three-dimensional thermal abuse model for lithium-ion cells, *J. Power Sources* 170 (2007) 476–489, <https://doi.org/10.1016/j.jpowsour.2007.04.018>.
- [28] R. Spotnitz, J. Franklin, Abuse behavior of high-power, lithium-ion cells, *J. Power Sources* 113 (2003) 81–100, [https://doi.org/10.1016/S0378-7753\(02\)00488-3](https://doi.org/10.1016/S0378-7753(02)00488-3).
- [29] A. Kriston, A. Podias, I. Adanouj, A. Pfrang, Analysis of the effect of thermal runaway initiation conditions on the severity of thermal runaway—numerical simulation and machine learning study, *J. Electrochem. Soc.* 167 (2020) 090555, <https://doi.org/10.1149/1945-7111/ab9b0b>.
- [30] R. Srinivasan, P.A. Demirev, B.G. Carkhuff, S. Santhanagopalan, J.A. Jeevarajan, T. P. Barrera, Review—thermal safety management in Li-ion batteries: current issues and perspectives, *J. Electrochem. Soc.* 167 (2020) 140516, <https://doi.org/10.1149/1945-7111/abc0a5>.
- [31] X. Tang, X. Wei, H. Zhang, D. Li, G. Zhang, X. Wang, J. Zhu, H. Dai, Experimental and modeling analysis of thermal runaway for $\text{LiNi}_{0.5}\text{Mn}_{0.3}\text{Co}_{0.2}\text{O}_2$, *Int. J. Energy Res.* 45 (2021) 10667–10681, <https://doi.org/10.1002/er.6552>.
- [32] J.P. Neidhardt, D.N. Fronczeck, T. Jahnke, T. Danner, B. Horstmann, W.G. Bessler, A flexible framework for modeling multiple solid, liquid and gaseous phases in batteries and fuel cells, *J. Electrochem. Soc.* 159 (2012) A1528–A1542, <https://doi.org/10.1149/2.023209jes>.
- [33] T.D. Hatchard, D.D. MacNeil, A. Basu, J.R. Dahn, Thermal model of cylindrical and prismatic lithium-ion cells, *J. Electrochem. Soc.* 148 (2001) A755, <https://doi.org/10.1149/1.1377592>.
- [34] Z. Wang, W. Fan, P. Liu, Simulation of temperature field of lithium battery pack based on computational fluid dynamics, *Energy Proc.* 105 (2017) 3339–3344, <https://doi.org/10.1016/j.egypro.2017.03.764>.
- [35] R.D. Jilte, R. Kumar, Numerical investigation on cooling performance of Li-ion battery thermal management system at high galvanostatic discharge, *Eng. Sci. Technol. an Int. J.* 21 (2018) 957–969, <https://doi.org/10.1016/j.jestch.2018.07.015>.
- [36] T. Albrecht, S. Horswell, L.K. Allerston, N.V. Rees, P. Rodriguez, Electrochemical processes at the nanoscale, *Curr. Opin. Electrochem.* 7 (2018) 138–145, <https://doi.org/10.1016/j.colelec.2017.11.016>.
- [37] D.P. Finegan, S.J. Cooper, Battery safety: data-driven prediction of failure, *Joule* 3 (2019) 2599–2601, <https://doi.org/10.1016/j.joule.2019.10.013>.
- [38] M. Ragone, V. Yurkiv, A. Ramasubramanian, B. Kashir, F. Mashayek, Data driven estimation of electric vehicle battery state-of-charge informed by automotive simulations and multi-physics modeling, *J. Power Sources* 483 (2021) 229108, <https://doi.org/10.1016/j.jpowsour.2020.229108>.
- [39] S. Song, C. Fei, H. Xia, Lithium-ion battery SOH estimation based on XGBoost algorithm with accuracy correction, *Energies* 13 (2020) 812, <https://doi.org/10.3390/en13040812>.
- [40] H. Rauf, M. Khalid, N. Arshad, Machine learning in state of health and remaining useful life estimation: theoretical and technological development in battery degradation modelling, *Renew. Sustain. Energy Rev.* 156 (2022) 111903, <https://doi.org/10.1016/j.rser.2021.111903>.
- [41] E. Cripps, M. Pecht, A Bayesian nonlinear random effects model for identification of defective batteries from lot samples, *J. Power Sources* 342 (2017) 342–350, <https://doi.org/10.1016/j.jpowsour.2016.12.067>.
- [42] J.C. Álvarez Antón, P.J. García Nieto, F.J. de Cos Juez, F. Sánchez Lasheras, M. González Vega, M.N. Roqueñí Gutiérrez, Battery state-of-charge estimator using the SVM technique, *Appl. Math. Model.* 37 (2013) 6244–6253, <https://doi.org/10.1016/j.apm.2013.01.024>.
- [43] R.R. Richardson, M.A. Osborne, D.A. Howey, Gaussian process regression for forecasting battery state of health, *J. Power Sources* 357 (2017) 209–219, <https://doi.org/10.1016/j.jpowsour.2017.05.004>.
- [44] R.R. Richardson, M.A. Osborne, D.A. Howey, Battery health prediction under generalized conditions using a Gaussian process transition model, *J. Energy Storage* 23 (2019) 320–328, <https://doi.org/10.1016/j.est.2019.03.022>.
- [45] A. Widodo, M.C. Shim, W. Caesarendra, B.S. Yang, Intelligent prognostics for battery health monitoring based on sample entropy, *Expert Syst. Appl.* 38 (2011) 11763–11769, <https://doi.org/10.1016/j.eswa.2011.03.063>.
- [46] G.E. Box, G.M. Jenkins, G.C. Reinsel, *Time Series Analysis: Forecasting and Control*, fifth ed., John Wiley & Sons, n.d.
- [47] J. Liu, A. Saxena, K. Goebel, B. Saha, W. Wang, An adaptive recurrent neural network for remaining useful life prediction of lithium-ion batteries, *2010, Annu. Conf. Progn. Heal. Manag. Soc. PHM* (2010), 0–9.
- [48] T. Yamanaka, Y. Takagishi, T. Yamaue, A framework for optimal safety Li-ion batteries design using physics-based models and machine learning approaches, *J. Electrochem. Soc.* 167 (2020) 100516, <https://doi.org/10.1149/1945-7111/ab975c>.
- [49] A. Naha, A. Khandelwal, S. Agarwal, P. Tagade, K.S. Hariharan, A. Kaushik, A. Yadu, S.M. Kolake, S. Han, B. Oh, Internal short circuit detection in Li-ion batteries using supervised machine learning, *Sci. Rep.* 10 (2020) 1–10, <https://doi.org/10.1038/s41598-020-58021-7>.
- [50] J. Redmon, S. Divvala, R. Girshick, A. Farhadi, You only look once: unified, real-time object detection, *Proc. IEEE Comput. Soc. Conf. Comput. Vis. Pattern Recognit.* 2016–Decem (2016) 779–788, <https://doi.org/10.1109/CVPR.2016.91>.
- [51] M. Doyle, T.F. Fuller, J. Newman, Modeling of galvanostatic charge and discharge of the lithium/polymer/insertion cell, *J. Electrochem. Soc.* 140 (1993) 1526–1533, <https://doi.org/10.1149/1.2221597>.
- [52] J. Newman, W. Tiedemann, Potential and current distribution in electrochemical cells: interpretation of the half-cell voltage measurements as a function of reference-electrode location, *J. Electrochem. Soc.* 140 (1993) 1961–1968, <https://doi.org/10.1149/1.2220746>.
- [53] Y. Chen, J.W. Evans, Three-Dimensional thermal modeling of lithium-polymer batteries under galvanostatic discharge and dynamic power profile, *J. Electrochem. Soc.* 141 (1994) 2947–2955, <https://doi.org/10.1149/1.2059263>.
- [54] M. Doyle, J. Newman, A.S. Gozdz, C.N. Schmutz, J. Tarascon, Comparison of modeling predictions with experimental data from plastic lithium ion cells, *J. Electrochem. Soc.* 143 (1996) 1890–1903, <https://doi.org/10.1149/1.1836921>.
- [55] H. Ekström, G. Lindbergh, A model for predicting capacity fade due to SEI formation in a commercial graphite/LiFePO₄ cell, *J. Electrochem. Soc.* 162 (2015) A1003–A1007, <https://doi.org/10.1149/2.0641506jes>.
- [56] K.S. Hariharan, P. Tagade, S. Ramachandran, *Mathematical Modeling of Lithium Batteries*, Springer International Publishing, Cham, 2018, <https://doi.org/10.1007/978-3-319-03527-7>.
- [57] T. Katrašnik, I. Mele, K. Zelić, Multi-scale modelling of Lithium-ion batteries: from transport phenomena to the outbreak of thermal runaway, *Energy Convers. Manag.* 236 (2021) 114036, <https://doi.org/10.1016/j.enconman.2021.114036>.
- [58] B.S. Parimalam, A.D. MacIntosh, R. Kadam, B.L. Lucht, Decomposition reactions of anode solid electrolyte interphase (SEI) components with LiPF₆, *J. Phys. Chem. C* 121 (2017) 22733–22738, <https://doi.org/10.1021/acs.jpcc.7b08433>.
- [59] G. Qian, F. Monaco, D. Meng, S.-J. Lee, G. Zan, J. Li, D. Karpov, S. Gul, D. Vine, B. Stripe, J. Zhang, J.-S. Lee, Z.-F. Ma, W. Yun, P. Pianetta, X. Yu, L. Li, P. Cloetens, Y. Liu, The role of structural defects in commercial lithium-ion batteries, *Cell Reports Phys. Sci.* 2 (2021) 100554, <https://doi.org/10.1016/j.xcrp.2021.100554>.
- [60] M.R. Gerhardt, A.A. Wong, M.J. Aziz, The effect of interdigitated channel and land dimensions on flow cell performance, *J. Electrochem. Soc.* 165 (2018) A2625–A2643, <https://doi.org/10.1149/2.0471811jes>.
- [61] W. Liao, Statistical properties of solutions to the Navier-Stokes equation in the limit of vanishing viscosity, *J. Phys. Math. Gen.* 22 (1989) L737–L741, <https://doi.org/10.1088/0305-4470/22/15/004>.
- [62] Comsol Multiphysics® v. 5.6, COMSOL AB, 2021. Stock. Sweden.,(n.D. www.comsol.com).
- [63] S.M. Abd Elrahman, A. Abraham, A review of class imbalance problem, *J. Netw. Innov. Comput.* 1 (2013) 332–340. www.mirlabs.net/jnic/index.html.
- [64] D.A.V. Dyk, X.L. Meng, The art of data augmentation, *J. Comput. Graph. Stat.* 10 (2001) 1–50, <https://doi.org/10.1198/10618600152418584>.
- [65] S.G.K. Patro, K.K. sahu, Normalization: a preprocessing stage, *Iarjset* 2 (2015) 20–22, <https://doi.org/10.17148/iarjset.2015.2305>.
- [66] F. Herrera, F. Charte, A.J. Rivera, M.J. del Jesus, Multilabel classification, in: *Multilabel Classif.*, Springer International Publishing, Cham, 2016, pp. 17–31, https://doi.org/10.1007/978-3-319-41111-8_2.
- [67] O. Fagbohungbe, L. Qian, Benchmarking inference performance of deep learning models on analog devices, *Proc. Int. Jt. Conf. Neural Networks.* (2021-July) 1–9, <https://doi.org/10.1109/IJCNN52387.2021.9534143>, 2021.
- [68] K. Lin, Y. Zhao, X. Gao, M. Zhang, C. Zhao, L. Peng, Q. Zhang, T. Zhou, Applying a deep residual network coupling with transfer learning for recyclable waste sorting,

- Environ. Sci. Pollut. Res. 29 (2022) 91081–91095, <https://doi.org/10.1007/s11356-022-22167-w>.
- [69] M. Tan, Q.V. Le, EfficientNet: rethinking model scaling for convolutional neural networks, Int. Conf. Mach. Learn. (2019), <https://doi.org/10.48550/arXiv.1905.11946>.
- [70] K. Simonyan, A. Zisserman, Very deep convolutional networks for large-scale image recognition, 3rd Int. Conf. Learn. Represent. ICLR 2015 - Conf. Track Proc. (2015) 1–14.
- [71] K. He, X. Zhang, S. Ren, J. Sun, Deep residual learning for image recognition, in: Proc. IEEE Comput. Soc. Conf. Comput. Vis. Pattern Recognit. 2016-Decem, 2016, pp. 770–778, <https://doi.org/10.1109/CVPR.2016.90>.
- [72] G. Huang, Z. Liu, L. van der Maaten, K.Q. Weinberger, Densely connected convolutional networks, in: Comput. Vis. Pattern Recognit. Conf., 2017, <https://doi.org/10.48550/arXiv.1608.06993>.
- [73] A. Howard, M. Sandler, B. Chen, W. Wang, L.-C. Chen, M. Tan, G. Chu, V. Vasudevan, Y. Zhu, R. Pang, H. Adam, Q. Le, Searching for MobileNetV3, IEEE/CVF Int. Conf. Comput. Vis., IEEE, 2019, pp. 1314–1324, <https://doi.org/10.1109/ICCV.2019.00140>, 2019.
- [74] J. Xu, R.D. Deshpande, J. Pan, Y.-T. Cheng, V.S. Battaglia, Electrode side reactions, capacity loss and mechanical degradation in lithium-ion batteries, J. Electrochem. Soc. 162 (2015) A2026–A2035, <https://doi.org/10.1149/2.0291510jes>.
- [75] <https://ewwest.com/support/panasonic-ncr18650bd-datasheet.pdf>.
- [76] V. Jabbari, V. Yurkiv, M.G. Rasul, M.T. Saray, R. Rojaee, F. Mashayek, R. Shahbazian-Yassar, An efficient gel polymer electrolyte for dendrite-free and long cycle life lithium metal batteries, Energy Storage Mater. 46 (2022) 352–365, <https://doi.org/10.1016/j.ensm.2022.01.031>.
- [77] P. Ramadass, B. Haran, R. White, B.N. Popov, Mathematical modeling of the capacity fade of Li-ion cells, J. Power Sources 123 (2003) 230–240, [https://doi.org/10.1016/S0378-7753\(03\)00531-7](https://doi.org/10.1016/S0378-7753(03)00531-7).
- [78] X. Lin, J. Park, L. Liu, Y. Lee, A.M. Sastry, W. Lu, A comprehensive capacity fade model and analysis for Li-ion batteries, J. Electrochem. Soc. 160 (2013) A1701–A1710, <https://doi.org/10.1149/2.040310jes>.
- [79] C. Zu, H. Yu, H. Li, Enabling the thermal stability of solid electrolyte interphase in Li-ion battery, InfoMat 3 (2021) 648–661, <https://doi.org/10.1002/inf2.12190>.
- [80] I. Kandel, M. Castelli, The effect of batch size on the generalizability of the convolutional neural networks on a histopathology dataset, ICT Express 6 (2020) 312–315, <https://doi.org/10.1016/j.icte.2020.04.010>.
- [81] N. Buduma, N. Locascio, Fundamentals of Deep Learning: Designing Next-Generation Machine Intelligence Algorithms, first ed., O'Reilly Media, Inc., 2017. <https://dl.acm.org/doi/10.5555/3161223>.
- [82] T. Saranya, C. Deisy, S. Sridevi, K.S. Muthu, M.K.A.A. Khan, Performance Analysis of First Order Optimizers for Plant Pest Detection Using Deep Learning, 2022, pp. 37–52, https://doi.org/10.1007/978-3-031-24367-7_4.
- [83] C.P. Papageorgiou, M. Oren, T. Poggio, A general framework for object detection, in: Sixth Int. Conf. Comput. Vis. (IEEE Cat. No.98CH36271), Narosa Publishing House, n.d.: pp. 555–562. <https://doi.org/10.1109/ICCV.1998.710772>.